*Electronic Supplementary Information (ESI)*

# $BiVO_4/Bi_2Mo_2O_9$ heterostructure towards oriented charge transfer for efficient photoelectrochemical water oxidation

Yuli Xiong[a*], Nan Zhou[a], Yuting Zhou[a], Bo Peng[a], Yuting Cui[a], Peng Yu[a]*, Zhenxiang Cheng[b]*

[a] College of Physics and Electronic Engineering, Chongqing Normal University, Chongqing 401331, P. R. China.

[b] Institute for Superconducting and Electronic Materials, Faculty of Engineering and Information Sciences, University of Wollongong, Innovation Campus, Squires Way, North Wollongong, NSW 2500, Australia.

Corresponding authors: ylxiong@cqnu.edu.cn (Y. Xiong), pengyu@cqnu.edu.cn (P. Yu), cheng@uow.edu.au (Z. Cheng).

**Keywords:** $BiVO_4/Bi_2Mo_2O_9$, interfacial interaction, charge transfer, solar energy, photoelectrochemical

# 1. Experimental Section

## 1.1 *Material characterizations*

The crystalline phases of the samples were determined by X-ray power diffraction (XRD) using a Shimadzu ZD-3AX diffractometer with CuKα radiation (λ = 1.5418 Å) at a scan rate of 2° per min in the angular range from 5° to 90°. The morphology and high-resolution microstructure images were observed through a field emission scanning electron microscope (FE-SEM, Hitachi, Regulus 8220) and a transmission electron microscopy (TEM, Talos F200S, 200kV) separately. The UV-Vis light absorption spectra were record with a spectrophotometer (UV-3600, Shimadzu) in the region of 300 – 800 nm. Room temperature photoluminescence (PL) measurement were carried out with a fluorescence spectrometer (Cary eclipse) with an excitation wavelength of 360 nm. The time-resolved PL measurement was carried out with Edinburgh FS5 with an excitation wavelength of 365 nm. The surface composition and chemical states analysis was carried out by an X-ray photoelectron spectroscopy (XPS, ESCALab250).

## 1.2 *Photoelectrochemical measurements*

Electrochemical tests were carried out using a Zahner Zennium electrochemical workstation operated in a standard three-electrode configuration, with a photoelectrode (1 $cm^2$) used as the working electrode. Meanwhile, a Pt coil (diameter is 1 mm, length is 5 cm) served as the counter electrode, an Ag/AgCl electrode (saturated KCl) used as the reference electrode. In a typical experiment, 0.2 M KPi with/without 0.5 M $Na_2SO_3$ as a hole scavenger was used as the electrolyte. The photo-response of the synthesized electrodes were measured under front-side illumination by a 300 W Xenon arc lamp

(NBet HSX-F300, China) equipped with an AM 1.5G filter (Ceaulight). The intensity of the light source was calibrated with a UV enhanced silicon photo-detector (Newport, Models 1916C and 818-UV) to simulate AM 1.5 illumination (100 mW $cm^{-2}$). For all the samples, a scan rate of 25 mV $s^{-1}$ used for the photocurrent-voltage (*J*-V) character. A photocurrent stability test was performed at a fixed bias potential of 1.23 V vs RHE under illumination. And the incident photon to current efficiency (IPCE) performance was performed at a fixed bias potential of 1.23 V vs RHE under illumination. Mott-Schottky plots were obtained in the electrolyte of 0.2 M KPi under illumination at an ac frequency of 500 and 1000 Hz. The carrier concentration and the flat potential can be estimated by the following equation:

$$(A_s/C_{bulk})^2 = (2/e\varepsilon\varepsilon_0 N_d)[V - V_{FB} - k_B T/e] \quad (1)$$

Where $A_s$ is the efficient area of electrode, $C_{bulk}$ is the space charge capacitance, ε is the dielectric constant of the samples, $\varepsilon_0$ is the permittivity under vacuum ($8.85 \times 10^{-12}$ $C^2$ $J^{-1}$ $m^{-2}$), $N_d$ is the carrier density of the samples, V is the applied potential, $V_{FB}$ is the flat band potential, $k_B$ is the Boltzmann constant ($1.38 \times 10^{-23}$ J $K^{-1}$), T (298 K) is the absolute temperature, and e is the electron charge ($1.602 \times 10^{-19}$ C).

The measured potential versus Ag/AgCl was converted to RHE potential by the Nernst equation

$$E_{RHE} = E_{Ag/AgCl} + 0.0591\ pH + 0.1976 \quad (2)$$

The photocurrent density arising from PEC performance ($J_{water}$) can be described as follows:

$$J_{water} = J_{abs} \times \eta_{sep} \times \eta_{oxi} \quad (3)$$

where $J_{abs}$ is the photocurrent density when completely converting the absorbed photons into current (i.e., APCE = 100%). $\eta_{sep}$ is the efficiency of charge separation and $\eta_{oxi}$ is the efficiency of surface oxidation kinetics. Adding 0.5 M $Na_2SO_3$ to the electrolyte can completely suppress the surface recombination of charge carriers without influencing the charge separation in the electrode bulk (i.e., $\eta_{oxi}$ = 100%). Therefore, $\eta_{sep}$ and $\eta_{oxi}$ can be expressed as follows:

$$\eta_{sep} = J_{sulfite} / J_{abs} \quad (4)$$

$$\eta_{oxi} = J_{water} / J_{sulfite} \quad (5)$$

where $J_{water}$ is the photocurrent density for water oxidation; $J_{sulfite}$ is the photocurrent density for sulfite oxidation. By estimating the overlapped areas between the AM 1.5G illumination, assuming APCE = 100%, the $J_{abs}$ of $Bi_2Mo_2O_9$ and $BiVO_4/Bi_2Mo_2O_9$ photoanodes are derived to be around 1.7 and 2.2 mA $cm^{-2}$.

## 2. Figures

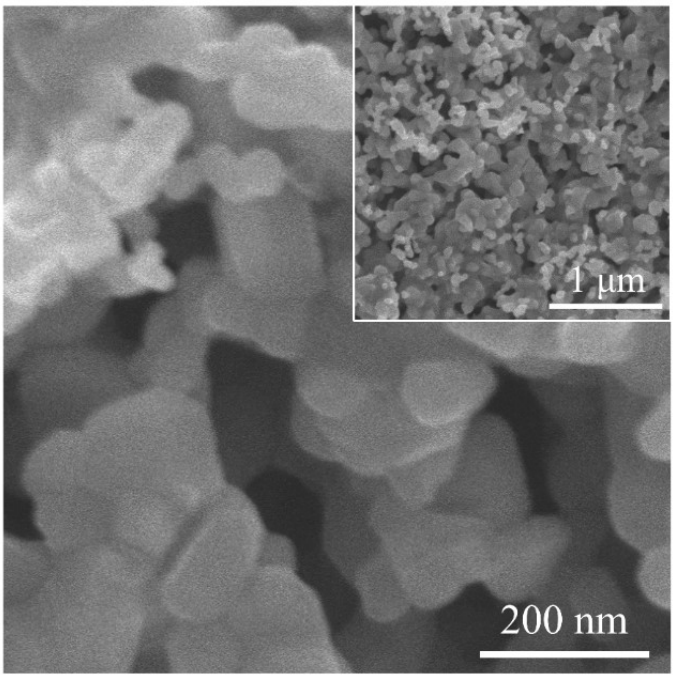


**Figure S1**. Top view SEM images of $Bi_2Mo_2O_9$, inset is the low magnification view.

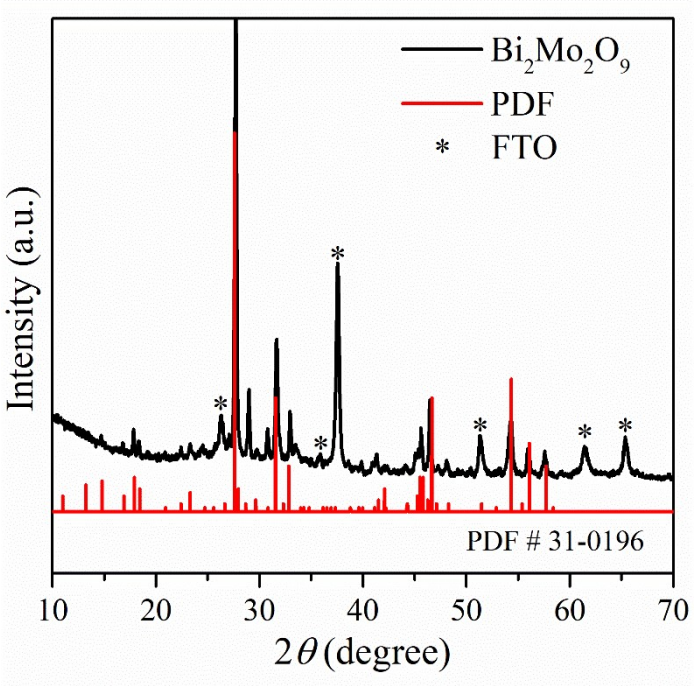


**Figure S2**. XRD spectra of $Bi_2Mo_2O_9$ and the FTO substrate.

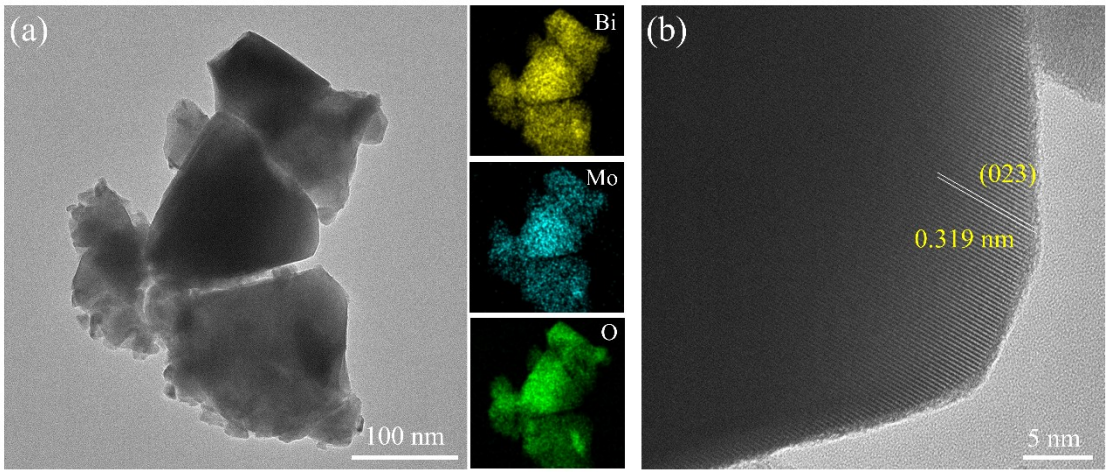


**Figure S3**. (a) TEM and the corresponding EDS elemental mappings of $Bi_2Mo_2O_9$, (b) HRTEM image of $Bi_2Mo_2O_9$.

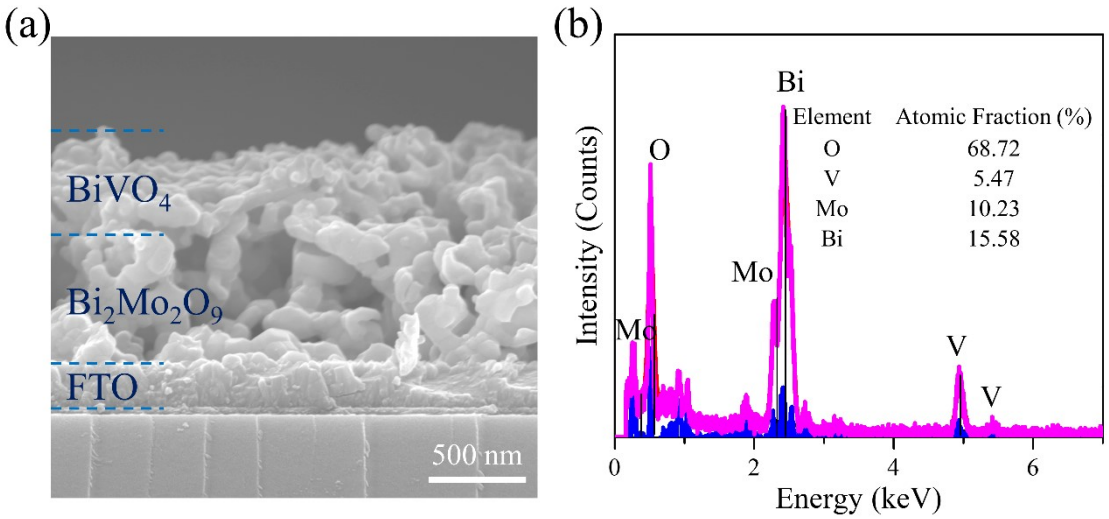


**Figure S4**. (a) The cross-sectional SEM of $BiVO_4/Bi_2Mo_2O_9$, the thickness of outer layer $BiVO_4$ and inner layer $Bi_2Mo_2O_9$ is around 400 nm and 600 nm. (b) TEM-corresponding EDX spectra of $BiVO_4/Bi_2Mo_2O_9$.

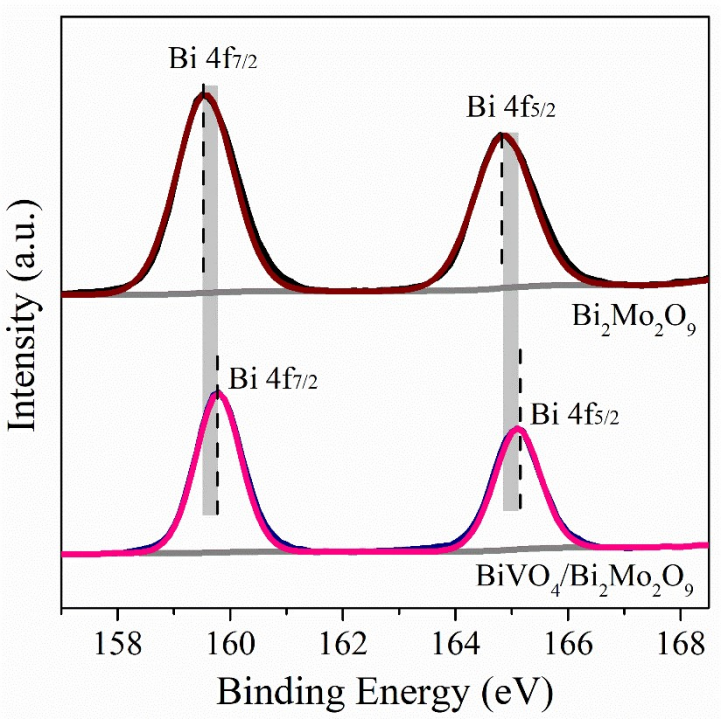


**Figure S5**. The high-resolution XPS spectra of Bi 4f for $Bi_2Mo_2O_9$ and $BiVO_4/Bi_2Mo_2O_9$.

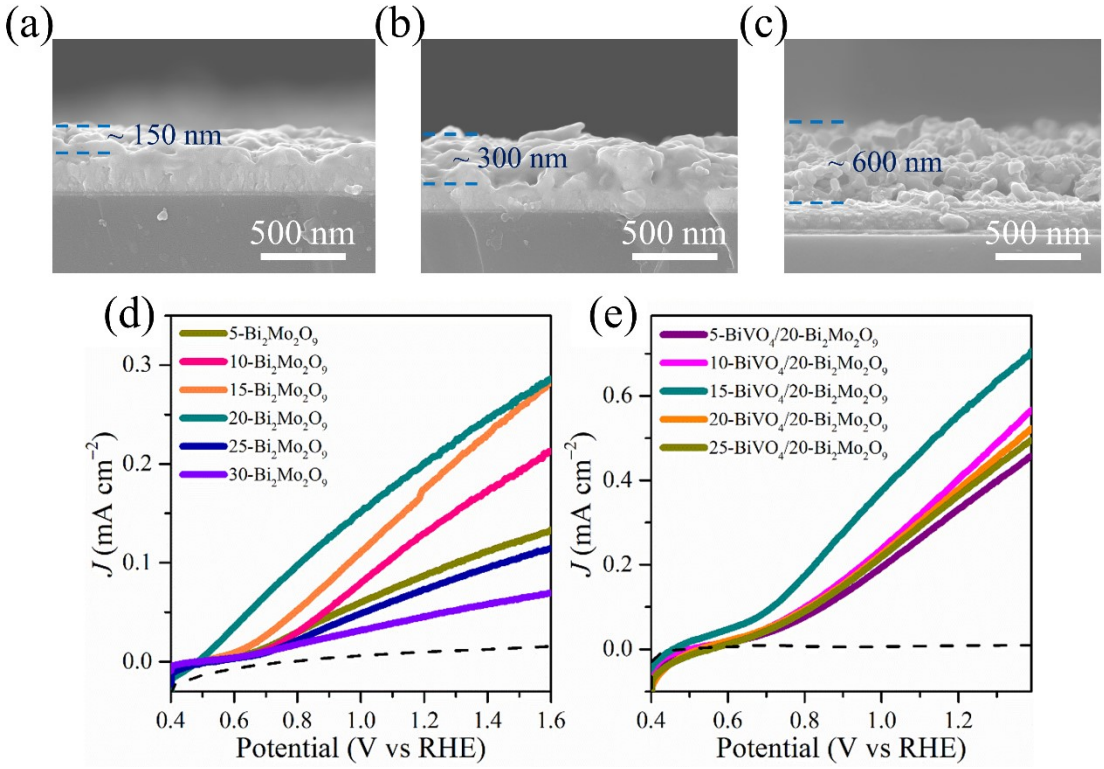


**Figure S6**. The cross-sectional SEM images of (a) 5-$Bi_2Mo_2O_9$, (b) 10-$Bi_2Mo_2O_9$, and (c) 20-$Bi_2Mo_2O_9$, the results suggest the thickness is around 150 nm, 300, and 600 nm. (d) Photocurrent of 5-$Bi_2Mo_2O_9$ (5 represent SILAR cycle numbers), 10-$Bi_2Mo_2O_9$, 15-$Bi_2Mo_2O_9$, 20-$Bi_2Mo_2O_9$, 25-$Bi_2Mo_2O_9$, and 30-$Bi_2Mo_2O_9$ photoanodes in 0.2 M KPi solution (pH 7.0) under AM 1.5G illumination (100 mW $cm^{-2}$) for PEC water oxidation. (e) The linear scanning voltammetry plots of $BiVO_4$/$Bi_2Mo_2O_9$ with different $BiVO_4$ thickness.

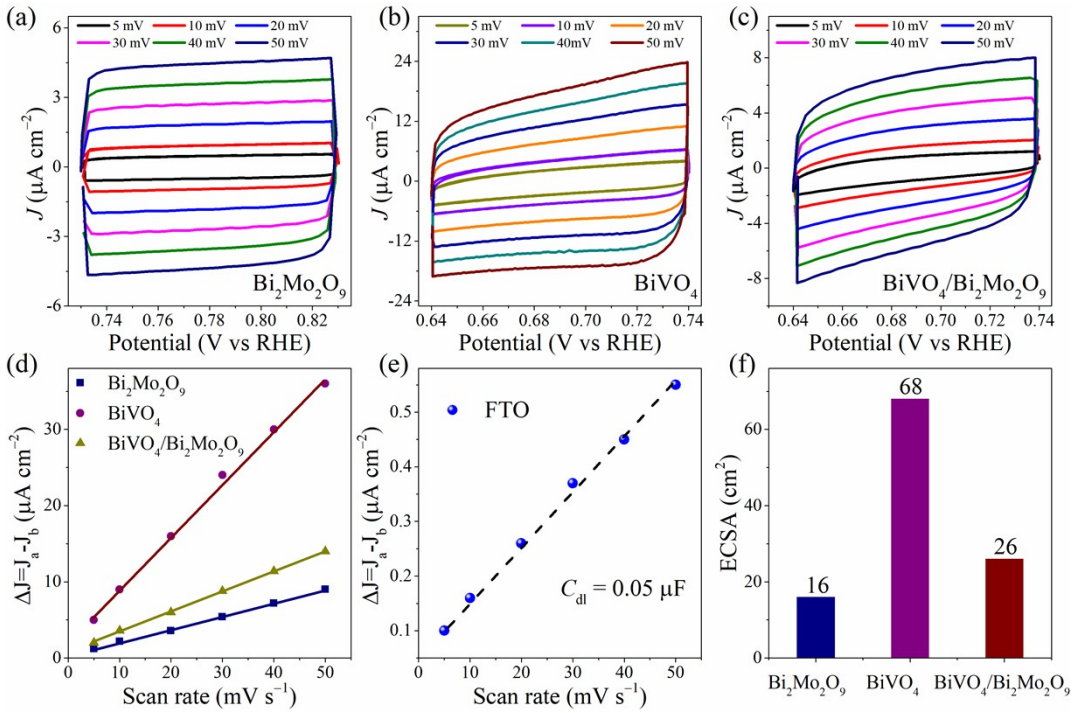


**Figure S7.** Cyclic voltammogram (CV) scans of (a) $Bi_2Mo_2O_9$, (b) $BiVO_4$, and (c) $BiVO_4/Bi_2Mo_2O_9$ in 0.2 M KPi solution, and the scanning rate is 5, 10, 20, 30, 40, and 50 mV $s^{-1}$, respectively. (d) Charge current density difference ($\Delta J = J_a - J_c$; $J_a$ and $J_c$ is the positive and negative current at 0.78 V vs RHE for $Bi_2Mo_2O_9$, 0.69 V vs RHE for $BiVO_4$, and 0.69 V vs RHE for $BiVO_4/Bi_2Mo_2O_9$) plotted against scan rates for various samples. (e) $\Delta J$ plotted against scan rates for the FTO substrate for the determination of special capacitance ($C_s$) at 0.6 V vs RHE. (f) The ECSA for these samples, which was estimated from the electrochemical double-layer capacitance ($C_{dl}$) by measuring $CV_s$ in a non-Faradaic region. The $C_{dl}$ values were determined from the slope of anodic-cathodic current density difference divided by two versus the scan rate. Therefore, the $C_{dl}$ value for the $Bi_2Mo_2O_9$, $BiVO_4$ and $BiVO_4/Bi_2Mo_2O_9$ is approximately 0.8, 3.4 and 1.3 μF $cm^{-2}$, respectively, and the $C_s$ of FTO is 0.05 μF $cm^{-2}$. The ECSA was calculated by using the equation: ECSA = $C_{dl}$ / $C_s$.

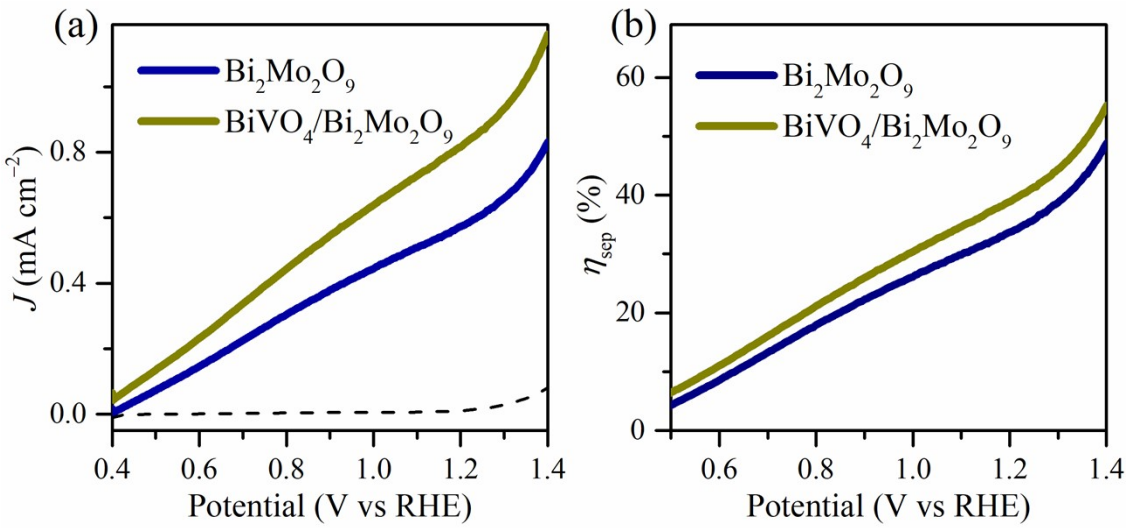


**Figure S8**. (a) Photocurrent density of $Bi_2Mo_2O_9$ and $BiVO_4/Bi_2Mo_2O_9$ in 0.2 M KPi with 0.5 M $Na_2SO_3$ solution. (b) Charge separation efficiency of these samples.

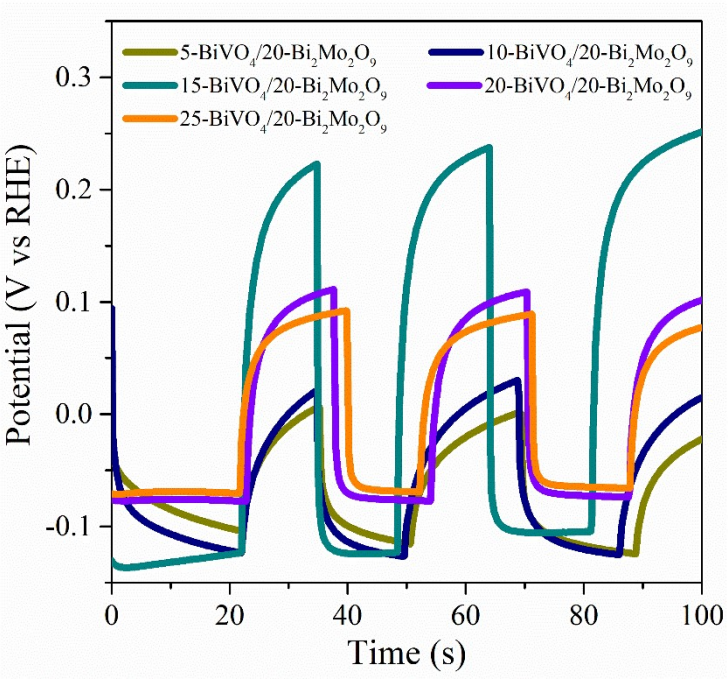


**Figure S9**. The open-circuit potential decay curves of all samples.

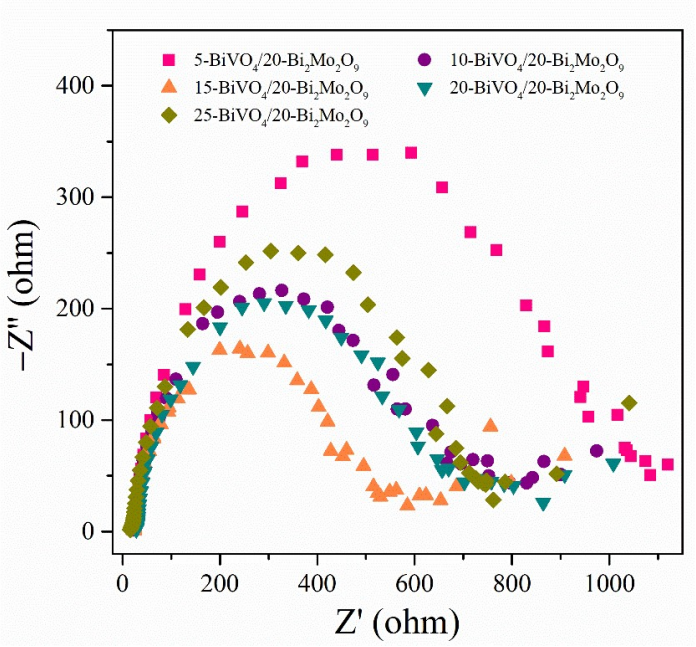


**Figure S10.** EIS tests of different photoanodes under AM 1.5 G illumination.

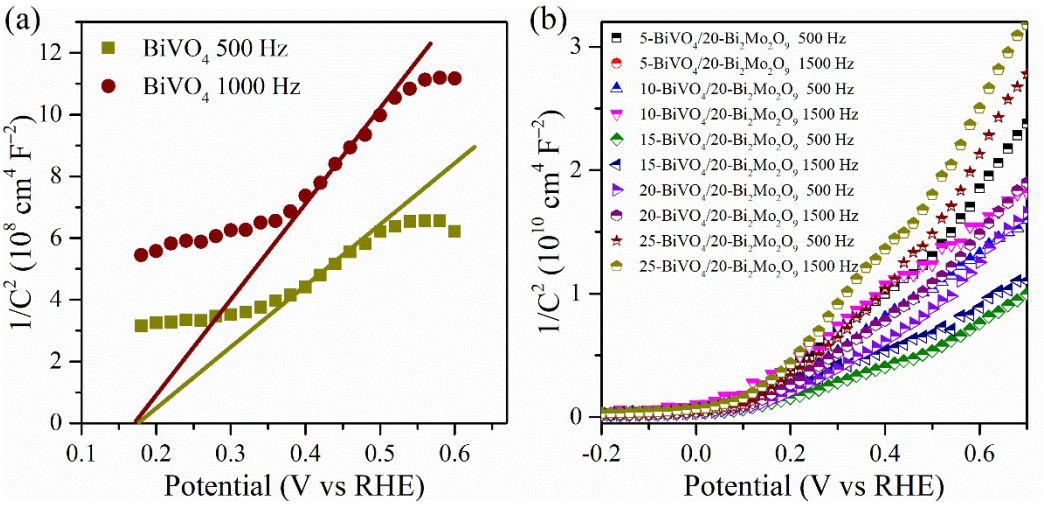


**Figure S11**. (a) Mott–Schottky curves of $BiVO_4$ under different frequencies in dark, (b) Mott–Schottky curves of different $BiVO_4/Bi_2Mo_2O_9$ photoanodes under different frequencies in dark. The $BiVO_4$ has a lower slope, indicating the higher carrier density in dark. However, under light illumination, due to the sluggish charge transfer dynamic and fast charge recombination, the photocurrent of bare $BiVO_4$ is low. To enhance the charge transfer rate, we constructed the $BiVO_4/Bi_2Mo_2O_9$ heterostructure.

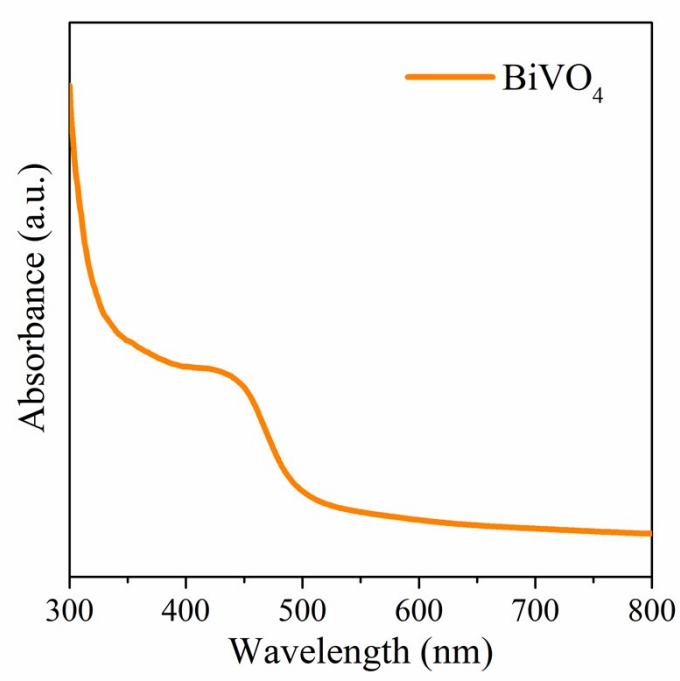


**Figure S12**. UV-Vis absorption spectrum of $BiVO_4$.

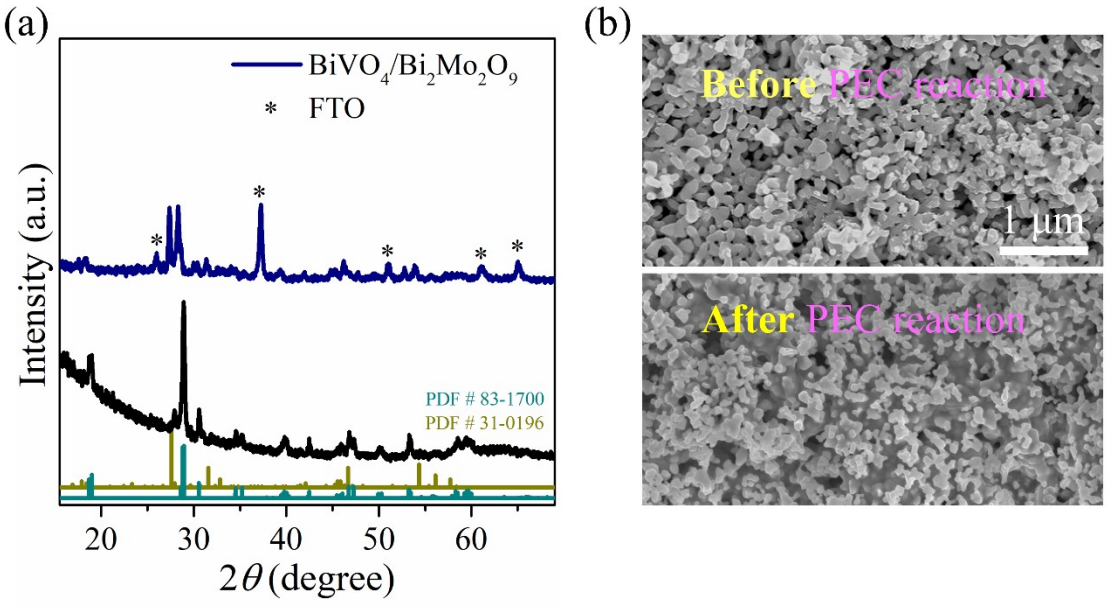


**Figure S13.** (a) XRD pattern of $BiVO_4/Bi_2Mo_2O_9$ heterostructure before/after PEC stability tests. (b) SEM image of $BiVO_4/Bi_2Mo_2O_9$ photoanodes before/after PEC reactions.

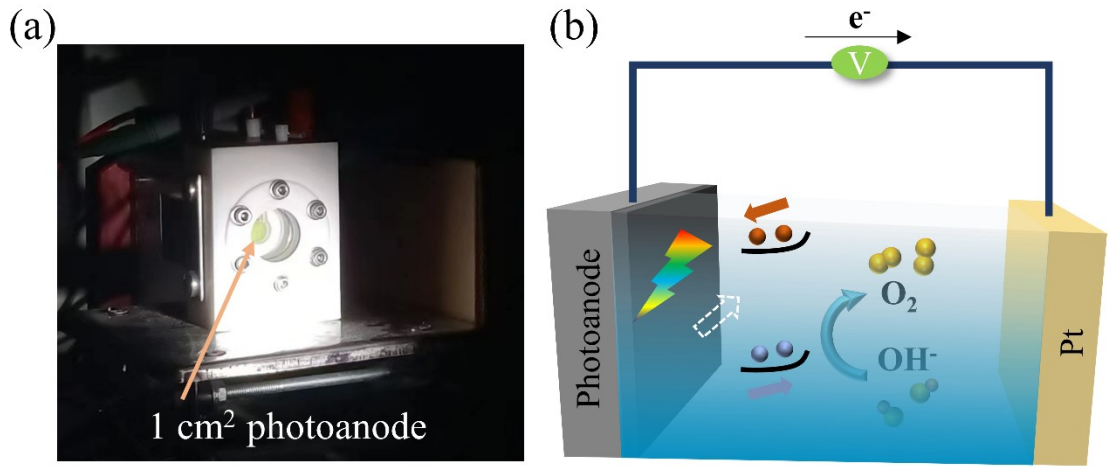


**Figure S14**. (a) Physical setup of the PEC cell, the solar light is illuminated by front direction. For this cell, the reaction surface of photoanode is fixed to 1 $cm^2$ by a Teflon plastic circular gasket. (b) Schematic of the PEC water oxidation (AM 1.5G illumination, 100 mW $cm^{-2}$).

**Table S1.** PEC performances of different photoanodes for water oxidation.

| | $Bi_2Mo_2O_9$ | $BiVO_4/Bi_2Mo_2O_9$ |
|---|---|---|
| Onset potential (V) | 0.55 | 0.41 |
| $J$ (mA $cm^{-2}$) | 0.18 | 0.61 |
| $\eta_{sep}$ | 35% | 41% |
| $\eta_{oxi}$ | 30.2% | 70.1% |
| Photovoltage (mV) | 150 | 340 |

$\eta_{sep}$: charge separation efficiency (at 1.23 V vs RHE)

$\eta_{ox}$: oxidation kinetics efficiency (at 1.23 V vs RHE)

**Table S2.** ICP tests of $BiVO_4/Bi_2Mo_2O_9$ photoanodes in 20 ml 5% $HNO_3$ solution, the detected elements including Bi, V, O, and Mo elements. 1 $cm^2$ of all photoanodes were used, the weight of each sample is ~2 mg.

| Samples | Atomic concentration (μmol $L^{-1}$) | | | | Atomic ratio of Bi:Mo:V:O |
|---|---|---|---|---|---|
| | Bi | Mo | V | O | |
| $BiVO_4/Bi_2Mo_2O_9$ (before *J*-t test) | 13.5 | 8.8 | 4.7 | 59.61 | 1:0.65:0.34:4.4 |
| $BiVO_4/Bi_2Mo_2O_9$ (after *J*-t test) | 13.4 | 8.3 | 4.5 | 59.67 | 1:0.65:0.34:4.5 |

**Table S3.** Relevant works of photocurrent enhancement by bismuth molybdate based photoelectrodes at 1.23 V vs RHE.

| Sample | Electrolyte | Photocurrent | Ref. |
|---|---|---|---|
| $Bi_2Mo_2O_9$–$Bi_2MoO_6$ | 0.1 M $Na_2SO_4$ | 0.22 mA $cm^{-2}$ | [1] |
| $Bi_2MoO_6$@$Bi_2Mo_2O_9$ | 0.5 M KPi | 0.16 mA $cm^{-2}$ | [2] |
| W doped $Bi_2MoO_6$ | 0.1 M $Na_2SO_4$ | 0.11 mA $cm^{-2}$ | [3] |
| $Bi_2MoO_6/TiO_2$ | 0.1 M KOH | 0.35 mA $cm^{-2}$ | [4] |
| $Bi_2MoO_6/Bi_2S_3$ | 0.1 M $Na_2SO_4$ | 1.4 mA $cm^{-2}$ | [5] |
| $BiVO_4/Bi_2Mo_2O_9$ | 0.2 M KPi | 0.61 mA $cm^{-2}$ | **This work** |

## References

[1] S. Baduri, D. Sariket, D. Raya, S. Ghosh, J. K. Singh, H-S. Lee, C. Bhattachary, Optimization of semiconductor–electrolyte interfacial phenomena for stable and efficient photoelectrochemical water oxidation behavior of $Bi_2Mo_2O_9$–$Bi_2MoO_6$ heterojunction. Electrochim. Acta 2021, 372, 137754.

[2] Y. Xiong, L. Yang, H. He, J. Wan, P. Xiao, W. Guo, Enhanced charge separation and transfer by $Bi_2MoO_6$@$Bi_2Mo_2O_9$ compound using SILAR for photoelectrochemical water oxidation. Electrochim. Acta 2018, 264, 26−35.

[3] M. Chakraborty, S. Ghosh, V. Mahalingam, Fe and W doped $Bi_2MoO_6$ nanoflakes: a promising material for efficient solar water splitting. Sustain. Energy Fuels 2020, 4, 1507−1514.

[4] Y. Lou, D. Qiu, S. Chen, H. Chen, L. Wang, Z. Hao, C. He, Y. Chen, X. Cui, Integrating $Bi_2MoO_6$ nanoflakes into $TiO_2$ photoanode for efficient charge separation in photoelectrochemical water splitting. J. Environ. Chem. Eng. 2023, 11, 111215.

[5] N. Le, N. T. N. Truong, N. H. Lam, A. M. Tamboli, M. S. Tamboli, M. R. Pallavolu, C. D. Kim, J. Jung, J. H. Jung, Direct growth of $Bi_2S_3$ nanorods onto the $Bi_2MoO_6$ nanoflakes: A promising heterostructure for efficient photoelectrochemical water-splitting application. FlatChem 2023, 37, 100468.